
Multidimensional Analysis of Direct-Drive, Plastic-Shell Implosions on OMEGA

Introduction

In direct-drive inertial confinement fusion (ICF),¹ nominally identical beams heat and compress a nearly spherical shell containing low-density gas. The high-density shell is unstable due to the Rayleigh–Taylor instability (RT)² at the ablation surface when the low-density blowoff plasma accelerates it. The target becomes RT unstable again, but at the inner fuel–shell interface or inner shell surface, later in the implosion when the lower-density gas decelerates the cold shell. Nonuniformities associated with the target, beam-to-beam power imbalance, and the individual beams seed this instability growth during both acceleration and deceleration phases. This compromises the uniformity of compression and degrades target performance.

Direct-drive-ignition designs require a cryogenic DT-ice layer imploded by a “shaped” pulse, with a long, low-intensity foot and a relatively slow rise to peak intensity.³ This article discusses warm, plastic-shell targets^{4,5} imploded on the OMEGA⁶ laser with a 1-ns square pulse, characterized by an initial sharp rise to peak intensity. Plastic-shell implosions are more susceptible to instability growth than cryogenic targets during both the acceleration and deceleration phases. The in-flight aspect ratio (IFAR; defined as the ratio of the shell position to the shell thickness when the shell has moved about half the total acceleration distance) of plastic shells discussed in this article is between 80 and 110, significantly larger than the ignition-design IFAR of ~60 (Ref. 3). The number of e -foldings due to RT growth increases for a larger IFAR.⁷ Consequently, plastic shells are more unstable during the acceleration phase than cryogenic shells. Plastic shells have two unstable surfaces during the deceleration phase: the gas–plastic (fuel–shell) interface whose growth dominates for all wavelengths, and the rear shell surface where short-wavelength growth is reduced due to a finite-density scale length. In contrast, during the deceleration phase, cryogenic targets are unstable only at the rear shell surface where finite density scale lengths and ablation⁸ (in the case of ignition targets) can significantly reduce growth rates of $\ell > 50$, where ℓ is the Legendre mode number. Implosions of warm plastic shells,

however, offer the advantage that complementary information of the compressed core can be obtained due to the variety of gas-fill types (D₂, DT, D³He, etc.) and fill pressures. This variety is unavailable with ignition-scaled cryogenic targets. As a result, detailed verification of the multidimensional hydrodynamics due to the presence of target and laser asymmetries can be performed with plastic shells.

Experimental results from direct-drive plastic-shell implosions have been discussed previously in the literature. Meyerhofer *et al.*⁴ first presented experimental results to infer core conditions. Radha *et al.*⁵ first pointed out the presence of small-scale mix in these implosions. Complementary diagnostics⁶ were employed to confirm this observation. However, the role of small-scale mix on target yields remained an outstanding question. Recently, 2-D simulations were employed by Radha *et al.*⁵ to understand the role of laser and target nonuniformities on implosion performance. It was determined that small-scale mix is not the primary determinant of gross target performance as measured through yields. Instead, long ($\ell \leq 10$) and intermediate ($10 \leq \ell \leq 50$) wavelengths dominated performance for the thick, stable shells, and short wavelengths ($\ell \leq 50$) determined target performance for the thin, unstable shells. In this article, this latter work has been extended to include a larger range of target types and fill pressures. In addition, a wider range of observables is compared to simulation results. This work summarizes simulations of plastic-shell implosions using the methods described in Ref. 5.

Imperfect illumination and target roughness seed the nonuniformity growth of hydrodynamic instabilities in direct-drive implosions. The incident laser irradiation on the target includes nonuniformities that result from energy and power imbalances among the beams and from nonuniformities within each beam. The former results in long-wavelength ($\ell \leq 10$, where $\ell = 2\pi R/\lambda$ is the Legendre mode number, R is the target radius, and λ is the nonuniformity wavelength) perturbations that lead to deformations of the shell. The latter are manifest in the intermediate-wavelength ($10 < \ell \leq 50$) and short-wavelength ($\ell > 50$) nonuniformities that can lead to shell breakup

during the acceleration phase due to Rayleigh–Taylor growth. All of these sources of nonuniformity can lead to a disruption of final fuel assembly. Two-dimensional simulations of plastic-shell implosions that take these effects into account using the hydrodynamic code *DRACO*⁵ are presented here. The modeling of multidimensional hydrodynamics is verified, leading to increased confidence in the predictions of direct-drive ignition³ on the National Ignition Facility.⁹ Simulation results are consistent with experimental observations.

The following sections (1) describe one-dimensional shell dynamics and laser drive, followed by nonuniformity seeding; (2) discuss the effect of short-wavelength growth on shell stability along with the effect of shell stability on experimental observables; (3) compare results from 2-D simulations to experimental results; and (4) present conclusions.

Targets, Laser Drive, and Shell Dynamics

A variety of gas-filled plastic (CH) shells, with thicknesses varying from 15 μm to 27 μm [Fig. 102.34(a)], have been imploded on OMEGA. Four target configurations are primarily discussed in this article: 20- μm -thick, 15-atm-fill; 20- μm -thick, 3-atm-fill; 27- μm -thick, 15-atm-fill; and 27- μm -thick, 3-atm-fill. A 1-ns square pulse¹⁰ [Fig. 102.34(b)] with ~ 23 kJ of energy irradiates these targets with full beam smoothing [two-dimensional smoothing by spectral dispersion¹¹ (1-THz, 2-D SSD with one color cycle) with polarization smoothing (PS)¹²]. Simulations presented here are for targets irradiated using distributed phase plates (DPP's)¹³ that have a super-Gaussian order ~ 2.26 with a spot size (defined as the diameter that is $1/e$ of peak intensity) of 616 μm (SG3 phase plates).¹⁴ More recently, phase plates on OMEGA have been upgraded to a super-Gaussian order ~ 4.12 with a spot size of 716 μm (SG4 phase plates) that primarily reduces the $\ell \leq 50$ nonuniformity.¹⁴ Comparison of observables between the SG3 and SG4 phase plates will also be presented to confirm the effect of laser nonuniformity on observables.

Plastic shells can be filled with a variety of gases at differing pressures that, during the implosion, provide a variety of nuclear and charged particles to diagnose implosion characteristics. Observables shown in this article include the primary neutron yield from the D_2 reaction, the shell areal density (ρR) inferred from both the energy loss of the protons from the D^3He reaction¹⁵ and the energy loss of the elastically scattered protons from the CH in DT-filled targets,¹⁶ the neutron-averaged ion temperatures inferred from neutron time-of-flight measurements, and ion temperatures inferred from the ratio of the DD neutron to D^3He proton yields.¹⁵ Time-resolved ob-

servations of neutron production rates¹⁷ and x-ray image self-emission¹⁸ are also routinely obtained. All of these experimental observables will be compared with results of simulations.

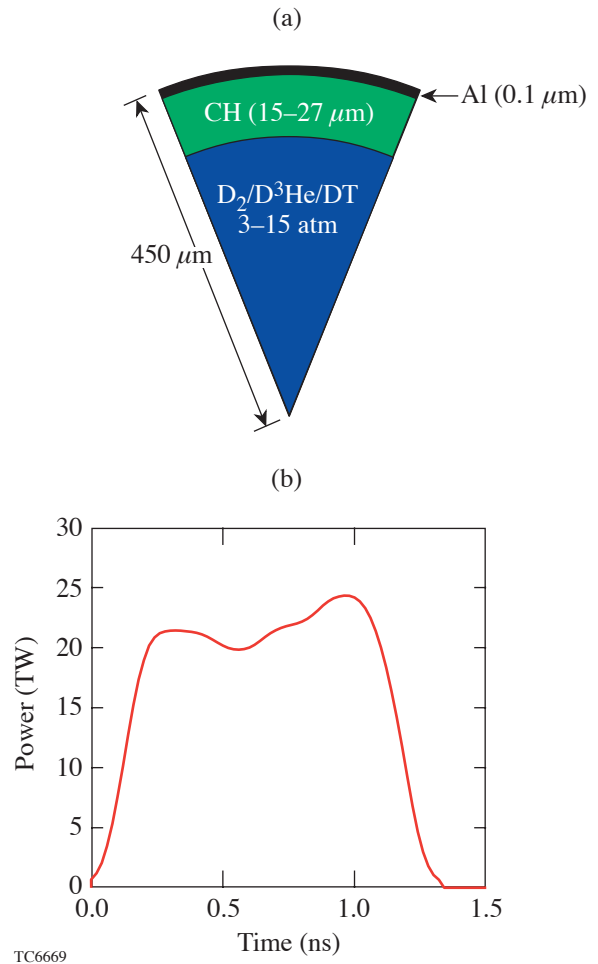


Figure 102.34

(a) Plastic-shell targets studied in this work. Two thicknesses—20 μm and 27 μm —with D_2 fills at 3 and 15 atm are considered. (b) The pulse shape (1 ns square) used to irradiate these targets sets the shell on a relatively high adiabat (~ 5).

The one-dimensional (1-D) dynamics of plastic shells can be divided into four stages: shock transit, acceleration, coasting, and deceleration. Shock dynamics simulated using the 1-D hydrodynamic code *LILAC*¹⁹ is shown in Fig. 102.35(a) as a contour plot of the gradient magnitude of the logarithm pressure, $|\partial \ln P / \partial r|$, as a function of Lagrangian coordinate and time. The target simulated in Fig. 102.35 has a shell thickness of 20 μm and encloses D_2 gas at a pressure of 15 atm. The dark lines correspond to shock trajectories. The dashed line is the trajectory of the fuel–shell interface. Since the rise

time of the laser is relatively fast (~ 200 ps), a strong shock is driven into the target. The rarefaction wave launched at the breakout of the shock (~ 0.4 ns) from the rear surface of the

shell reaches the ablation surface, launching a compression wave into the target. At this time, the shell accelerates inward and the ablation surface is subject to RT growth.²⁰ The compression wave travels down the decreasing density gradient and breaks out of the rear surface of the shell as a shock (at ~ 0.8 ns). The shocks meet in the gas (at ~ 1 ns) before reaching the center.

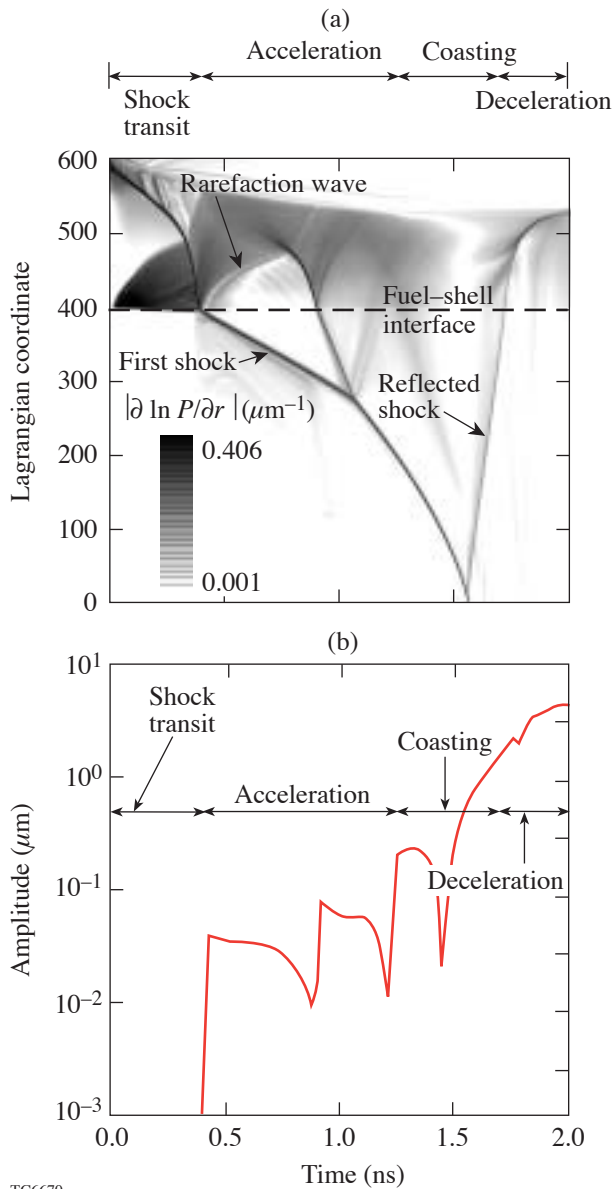


Figure 102.35

(a) Contour plot of the gradient magnitude of the natural log of the pressure for a $20\text{-}\mu\text{m}$ -thick CH shell enclosing 15 atm of D_2 gas. The y axis corresponds to the Lagrangian coordinate in the 1-D simulation. The darker contours correspond to shock trajectories. The dashed line is the fuel-shell interface. The duration of the four phases of the implosion (shock transit, acceleration, coasting, and deceleration) is also shown. (b) The growth of a single mode ($\ell = 30$) at the fuel-shell interface through the implosion. The interface is seeded primarily by the shock and grows significantly during the coasting phase.

The fuel-shell interface has a non-zero Atwood number ($A_T = 0.18$ for D_2 fills)⁵ and is unstable for all wavelengths. The growth of a single mode at the fuel-shell interface simulated using the code *DRACO*⁵ is shown in Fig. 102.35(b). The interface is primarily seeded by the shock (~ 0.4 ns). The acceleration phase occurs after shock transit until ~ 1.4 ns, during which feedthrough from the RT growth at the ablation surface plays an important role in increasing the nonuniformity at the fuel-shell interface. For the mode $\ell = 30$ [shown in Fig. 102.35(b)], the negative spikes for $t < 1.4$ ns correspond to repeated shock interactions with the interface. Significant growth of the interface occurs after the acceleration phase and during the coasting phase due to Bell-Plesset²¹ growth. This persists until the shock reflects from center and returns to the shell (~ 1.75 ns). This impulsive deceleration is followed by a period of continuous deceleration, when the fuel-shell interface is RT unstable due to pressure buildup in the gas. The RT-unstable interface distorts with bubbles of the lower-density fuel rising into the high-density plastic and spikes of the high-density CH falling into the lower-density fuel. Most observables for diagnosing implosion dynamics occur during this final phase of the implosion. Comparison of simulation to observations, therefore, provides an extremely stringent test of modeling perturbation growth and multidimensional fluid flow.

Nonuniformity Seeding

The nonuniformity sources seeding the instabilities at the ablation surface and the fuel-shell interface can be divided into three wavelength ranges for the analysis of these implosions. Long-wavelength modulations ($\ell \leq 10$) result in an overall deformation of the shell, whereas the intermediate ($10 < \ell \leq 50$) and short wavelengths ($\ell > 50$) result in a mass-modulated shell that can show considerable distortions including shell breakup. The time evolution of the long-wavelength nonuniformity sources due to imbalances between the OMEGA beams is modeled by overlapping the 60 beams on a sphere.⁵ Beam mispointing ($\sim 23\text{-}\mu\text{m}$ rms²²), beam mistiming ($\sim 12\text{-ps}$ rms is used in the calculation although $\sim 9\text{-ps}$ rms²³ is more typical of OMEGA), energy imbalance ($\sim 2.6\%$ ²²), and differences in the phase plates including azimuthal asymmetries are taken into account. These numbers are averaged over several

shots. The overlap is decomposed into spherical harmonics, and the amplitude of the corresponding Legendre mode is obtained by adding all the m -mode amplitudes in quadrature. The phase of the mode is chosen to be that of the $m=0$ spherical harmonic. These time-dependent amplitudes are used as the laser modulation input to the 2-D axisymmetric hydrodynamic code *DRACO*.

The amplitudes of the dominant modes at the ablation surface (defined as the outer $1/e$ point of maximum density) at the start of the acceleration phase are shown in Fig. 102.36(a). These amplitudes are seeds for RT growth during the acceleration phase. Also shown in Fig. 102.36(a) are the amplitudes due to target surface roughness²⁴ at the same time in the simulation. Figure 102.36(a) indicates that power imbalance is the larger of the two contributors to low-order nonuniformity.

Intermediate and shorter wavelengths are dominated by single-beam nonuniformity (through laser imprint²⁵). An analytical model²⁶ describing the DPP's is used to modulate the laser illumination on target. In addition, polarization smoothing reduces the amplitudes by $\sqrt{2}$ (Ref. 12), and smoothing by spectral dispersion¹¹ (1-THz, 2-D SSD with one color cycle) is also applied. These models are described in detail in Ref. 5. The resultant amplitudes at the ablation surface at the start of the acceleration phase are shown in Fig. 102.36(b). The ampli-

tudes decrease with increasing mode number. This is due to the earlier decoupling of the shorter wavelengths from the target and stabilization due to dynamic overpressure.²⁵

Effect of Shell Stability on Observables

Figure 102.37 shows density contours from multimode simulations that include only the effect of single-beam nonuniformity ($2 \leq \ell \leq 200$) for two CH-shell thicknesses [Fig. 102.37(a): 20 μm ; Fig. 102.37(b): 27 μm]. These contours are shown at the end of the acceleration phase. The 20- μm -thick shell, being less massive, has traveled a greater distance during acceleration and is considerably more distorted than the 27- μm -thick CH shell. The peak-to-valley variation in the center-of-mass radius for the 20- μm -thick shell is 6.6 μm at the end of the acceleration phase, significantly greater than the calculated 1-D shell thickness (defined as the distance between the $1/e$ points of maximum density in a spherically symmetric simulation) of $\sim 5 \mu\text{m}$, indicating shell breakup. The high-density regions are considerably distorted with portions of the shell at less than solid density. Therefore, short wavelengths play an important role in increasing the adiabat of the shell by introducing additional degrees of freedom for the fluid flow. This influences the compressibility of the shell and, therefore, quantities such as neutron yields and areal densities. In comparison, the 27- μm -thick implosion has an integral shell at the end of the acceleration phase with a

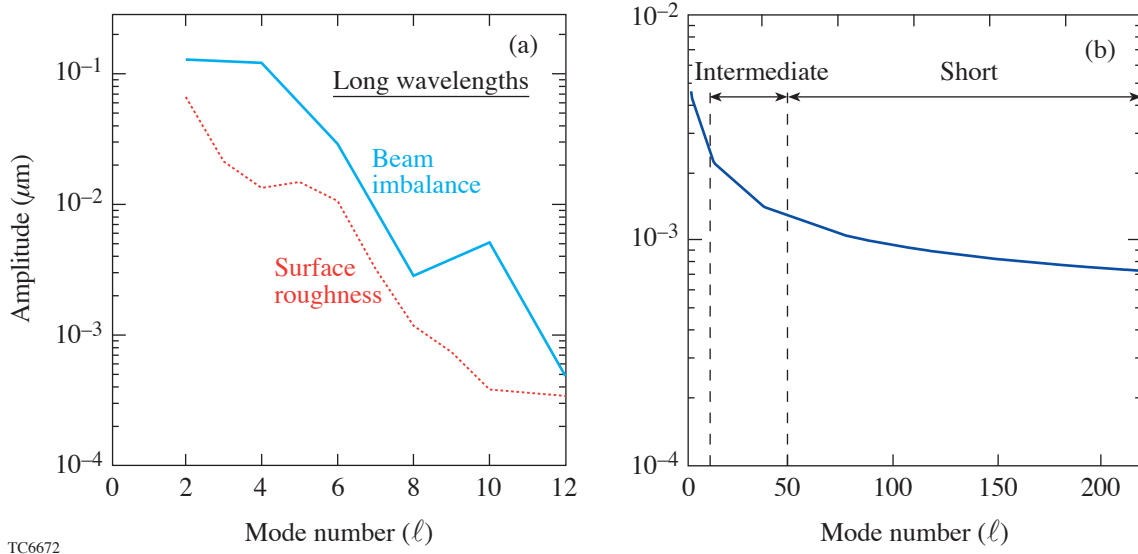


Figure 102.36 (a) Long-wavelength perturbations at the ablation surface due to beam imbalance (solid line) and surface roughness (dotted line) at the start of acceleration. Beam imbalance provides the larger contribution to long-wavelength nonuniformity seeds. (b) Imprint spectrum from single-mode simulations. Note that imprint efficiency decreases with increasing mode number.

peak-to-valley amplitude of $3.4 \mu\text{m}$ in the center-of-mass radius compared to a 1-D shell thickness of $\sim 6.8 \mu\text{m}$. To realistically model the effect of laser imprint, modes resolved up to $\ell \sim 400$ are required in the simulation.⁵ A reliable simulation of this type is numerically challenging. Instead, a stability postprocessor²⁷ to *LILAC* is used to confirm that the qualitative conclusions do not change, i.e., the integrity of the 20- μm -thick CH shell is severely compromised, whereas the 27- μm -thick CH shell is essentially intact when the full range of modes is included.

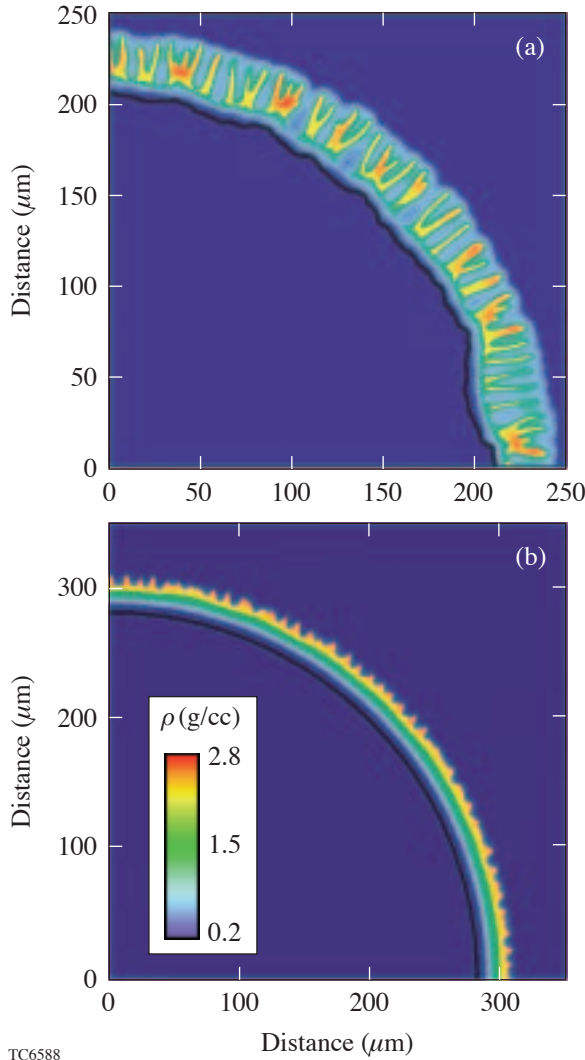


Figure 102.37 Density contours at the end of the acceleration phase for (a) a 20- μm -thick CH shell and (b) a 27- μm -thick CH shell from a multimode simulation of laser imprint. The solid lines correspond to the D_2 -CH interface. Note that the shell (indicated by the higher-density contours) is significantly more distorted for the 20- μm implosion than the 27- μm implosion.

When the severely distorted 20- μm -thick CH shell reassembles during the later stages of the implosion (around the time of the interaction of the reflected shock with the converging shell), the lower density due to shell breakup will result in a thicker shell than predicted with 1-D and a ρR that is lower than 1-D predictions. The thicker shell will influence neutron production rates as follows: Between the time of peak neutron production and peak compression (shown schematically in Fig. 102.38), the neutron rate decreases due to the falling temperature in the gas because of heat conduction and radiative losses. The subsequent decrease in the neutron-production rate occurs due to shell disassembly. If the shell is thicker due to nonuniformity growth, disassembly occurs later in the implosion. The time between the interaction of the reflected shock (which is very similar for both integral and severely distorted shells) and the shock breakout of the shell is given by $t_s = \Delta_{\text{sh}}/U_s$, where Δ_{sh} is the shell thickness and U_s is the shock speed. From Ref. 5, $U_s = \sqrt{E_{\text{kin}}/R_{\text{hs}}^2 \Delta_{\text{sh}} \rho_{\text{sh}}}$, where E_{kin} is the shell kinetic energy, R_{hs} is the radius of the hot spot, and ρ_{sh} is the shell density. Since E_{kin} is similar between the integral shell and the severely distorted shell implosion (only a small portion of the total energy goes into lateral flow in the

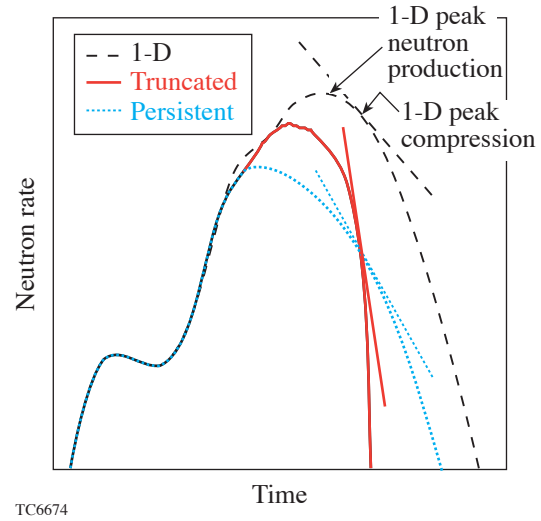


Figure 102.38 Schematics of a persistent neutron-production history and a truncated neutron-production history. In persistent neutron-production histories, burn follows 1-D (dashed) and then turns over (dotted). The rate of falloff near the peak is slower than in 1-D, as indicated by the lines drawn as tangents at peak compression. In truncated neutron-production histories, burn follows 1-D and then turns over rapidly near the peak with a distinct increase in the rate of falloff relative to 1-D (solid). The tangent line drawn at peak compression has a steeper slope compared to 1-D.

distorted shell implosion) and mass ($\propto R_{\text{hs}}^2 \Delta_{\text{sh}} \rho_{\text{sh}}$) is conserved, the shock velocity is similar in both cases; therefore, $t_s \propto \Delta_{\text{sh}}$ and is longer for the severely distorted shell, and disassembly is delayed. Consequently, neutron production falls less steeply than 1-D (Fig. 102.38, dashed line) in the implosion where shell stability is compromised (Fig. 102.38, dotted line). This is indicated in Fig. 102.38 by the decreased slope of the tangent line drawn at peak compression. For stable shells (27 μm), the shell thickness during neutron production is comparable to the 1-D thickness. In this case, the neutron-production rate will truncate (Fig. 102.38, solid line) primarily due to the RT-instability-induced mass flow into the colder bubbles near the fuel-shell interface.⁵ This is indicated by the increased slope of the tangent line drawn at peak compression.

Comparison of Simulations with Observables

The effect of the entire range of nonuniformities is modeled with two-mode simulations with mode numbers 4 and 20 used to represent the effect of long and intermediate wavelengths and three-mode simulations with modes 4, 20, and 200 used to represent all mode ranges. These simulations are performed on a 45° wedge. The initial amplitude for each mode is chosen from the amplitudes added in quadrature of a range of mode numbers (from the DPP and PS spectrum for $\ell = 20$ using modes between 15 and 40 as the mode range and using modes between 100 and 300 as the mode range for $\ell = 200$, and from the initial power balance and surface-roughness data for modes $2 < \ell \leq 10$ for mode $\ell = 4$). SSD is applied to $\ell = 200$ by reducing its initial amplitude by a factor $\sqrt{(t_c/t_D)}$, where t_c is the coherence time of mode 200 (~2 ps) and t_D is the decoupling time for this mode (~16 ps for the 1-ns square

pulse). This reduction factor is in agreement with measurements.²⁸ Density contours at peak neutron production in 2-D are shown for the two thicknesses in Fig. 102.39. The 2-D fuel-shell interface (solid black line) in both cases is significantly distorted compared to 1-D (dashed line). The peak density in the thinner shell is ~70% of the 1-D peak density compared to nearly 100% for the thick shell. This undercompression is due to shell breakup during the acceleration phase, as discussed in the previous section.

Neutron-production rates from these simulations are compared against 1-D rates (solid line) in Fig. 102.40 [Fig. 102.40(a): 20- μm -thick CH shell; Fig. 102.40(b): 27- μm -thick CH shell]. With low and intermediate modes alone (dashed line), burn truncation is evident for both shell thicknesses. In this case, the in-flight shell thickness is the same as the 1-D shell thickness. The addition of the short wavelength (dotted line) significantly influences the neutron-production rate for the 20- μm shell; the burn rate deviates from 1-D with a more gradual falloff. The short wavelength has only a marginal effect on the thicker shell. Similar trends are observed in experiments. The 1-D calculated and measured neutron-production rates are shown in Fig. 102.41 for three shell thicknesses. The 1-D neutron rates are temporally shifted to align the rise of neutron production with the rise of the measured rate curves. The required time shifts are within the uncertainties in absolute timing in the experiment. Burn truncation is evident for the thick shell case [Fig. 102.41(c)]; the tangent line has a steeper slope compared to 1-D, whereas, with decreasing shell thickness, neutron-production falls off less rapidly near the peak. Measurement and 1-D simulations from a 15- μm -thick CH implosion are

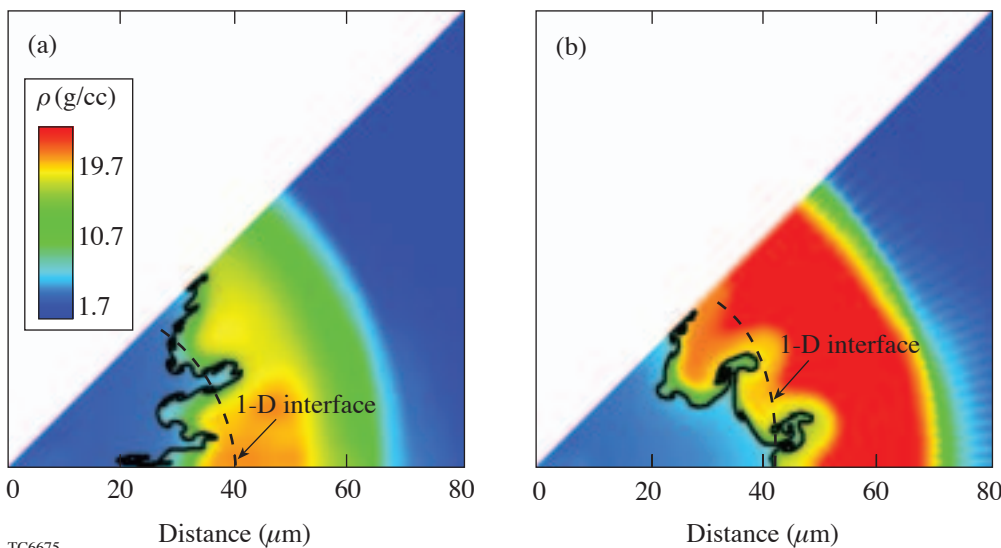


Figure 102.39 Density contours for simulations including the effect of all mode ranges at peak neutron production for (a) the 20- μm -thick CH shell and (b) the 27- μm -thick CH shell. The solid line is the fuel-shell interface. The peak density in (a) is ~70% of the 1-D peak density, whereas in (b) it is ~100% of 1-D peak density. This undercompression in the 20- μm -thick shell occurs due to shell instability during acceleration.

compared in Fig. 102.41(a). This shell should be even more compromised in its integrity than the 20- μm -thick CH shell. The measured rates show the expected trend: a more gradual falloff near the peak.

Simulated neutron-production rates for the 20- μm -thick CH shell with a 3-atm fill are shown in Fig. 102.42(a). Even though the shell is severely compromised during acceleration, burn truncation is evident in this case. Nonuniformity growth

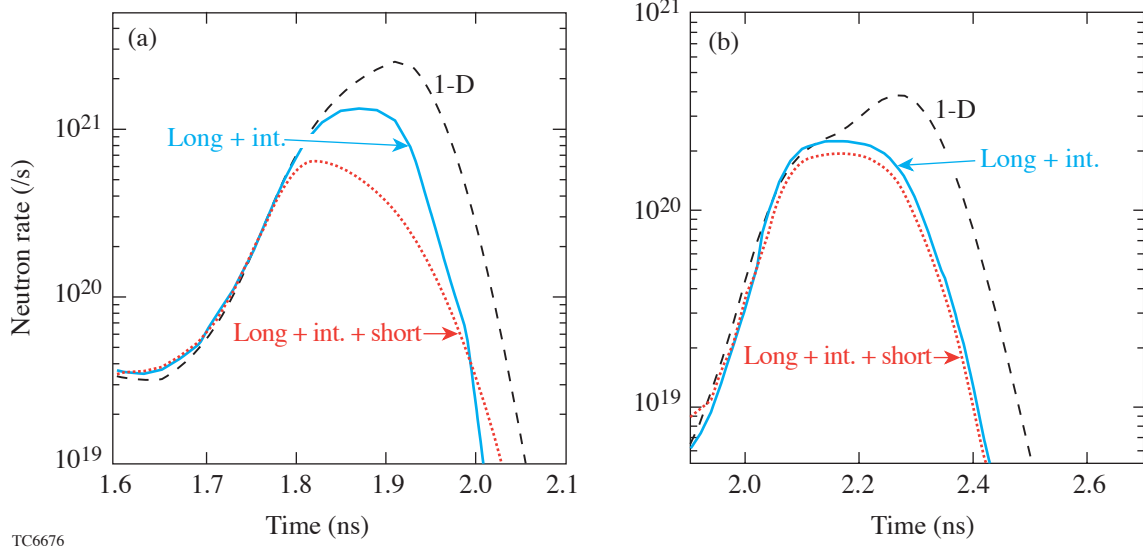


Figure 102.40

Neutron-production rates from the simulation including only low- and intermediate-mode numbers (dotted line) and the simulation including short wavelengths (solid line) compared to 1-D (dashed line) for (a) the 20- μm -thick CH shell and (b) the 27- μm -thick CH shell. Note that the inclusion of the shorter wavelengths in the simulation results in a less-steep fall of the neutron-production rate for the 20- μm implosion and retains burn truncation for the 27- μm case.

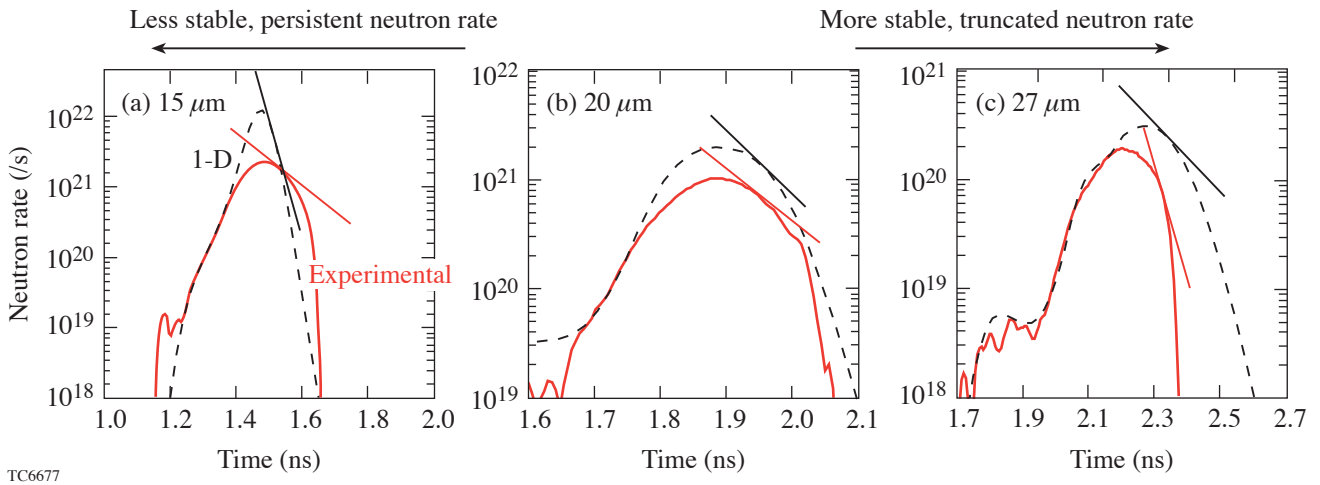


Figure 102.41

Comparison of calculated (1-D) neutron rates (dashed) with experiment (solid line) for (a) the 15- μm -thick implosion (shot 36100), (b) the 20- μm -thick implosion (shot 30628), and (c) the 27- μm -thick implosion (shot 22088). All implosions have a 15-atm fill. Burn truncation is evident for the 27- μm -thick implosion. The neutron-production rate persists and is almost as wide as 1-D for the 20- μm -thick implosion and wider than 1-D for the 15- μm -thick implosion.

at the interface compromises the core; at peak neutron production in 1-D (~1.85 ns), there is no clean core evident in the 2-D simulations, reducing the neutron rate significantly and resulting in truncation. Consistent with this simulation, burn truncation is evident in the measured neutron-production rates [Fig. 102.42(b)] when overlaid onto the 1-D simulation results.

Two-dimensional simulated primary neutron yields compare very favorably with measured values. Figure 102.43 shows the experimental yield⁴ normalized to the correspond-

ing 1-D yields (open circles) for the four target configurations: 20- μm -thick, 15-atm-fill; 20- μm -thick, 3-atm-fill; 27- μm -thick, 15-atm-fill; and 27- μm -thick, 3-atm-fill. Each point is this quantity averaged over many OMEGA shots. The error bars are the one-standard-deviation variation over these shots. All simulated values (solid symbols) compare well with observations.

Simulated neutron-averaged shell areal densities normalized to the 1-D values (solid) are shown in Fig. 102.44, comparing favorably with the experimentally inferred val-

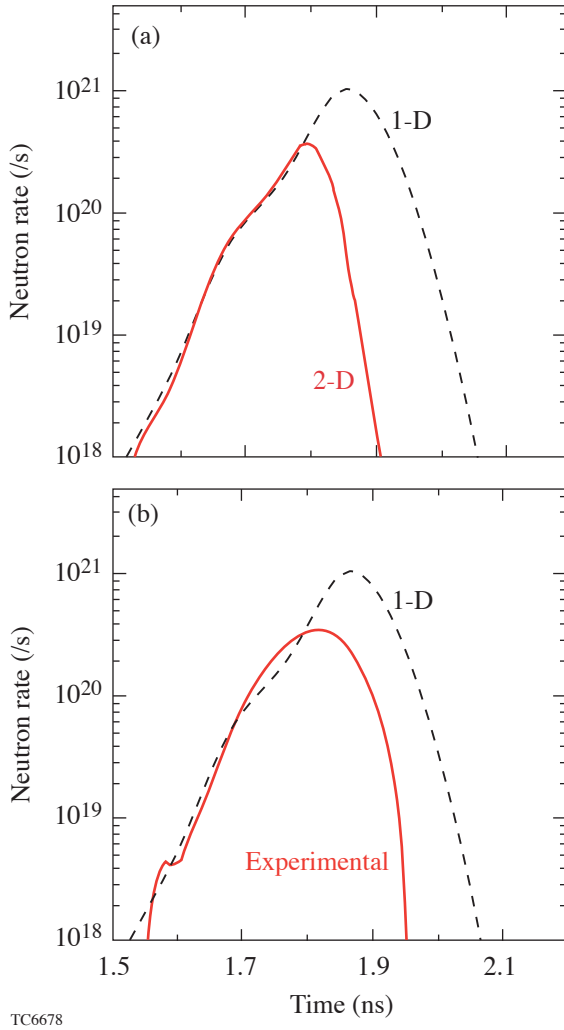


Figure 102.42 (a) Simulated neutron-production rates for the 20- μm -thick, 3-atm-fill implosion: 2-D (solid) and 1-D (dashed). Burn truncation is evident even though the shell is significantly distorted during acceleration because of the absence of a “clean” core early during deceleration. (b) Comparison of the 1-D simulation with measured neutron-production rate (shot 22864). The same trend of burn truncation is observed in experiment.

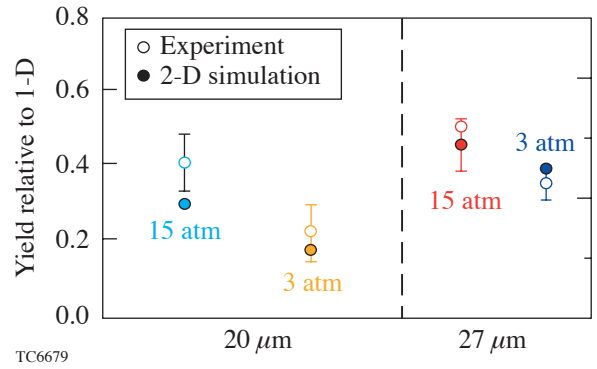


Figure 102.43 Yields relative to 1-D for four cases: 20- μm -thick, 15-atm-fill; 20- μm -thick, 3-atm-fill; 27- μm -thick, 15-atm-fill; and 27- μm -thick, 3-atm-fill (measured: open circles; 2-D: closed circles). Good agreement is obtained between experiment and simulation.

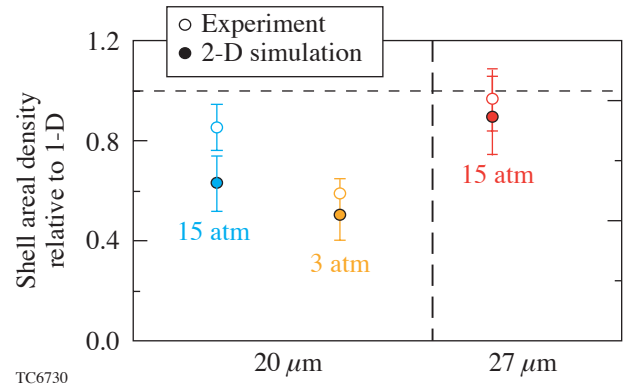


Figure 102.44 Neutron-averaged shell areal density relative to 1-D for the same four targets as in Fig. 102.43. Simulations are shown as the solid symbols. The “error bar” in the 2-D results is the one standard deviation in the variation in the polar angle areal density.

ues¹⁵ (open). The error bars associated with the simulation points are the one-standard-deviation polar-angle variation in the areal density. There is no data for the 27- μm -thick, 3-atm-fill implosion.

Experimental neutron-averaged ion temperatures⁴ inferred from neutron time of flight are shown in Fig. 102.45 (open circles). Experimentally inferred ion temperatures are systematically higher than those simulated (solid). Reasons for this systematic deviation are being investigated currently. Ion temperatures from the measured DD neutron to D³He proton yield ratios¹⁵ are also shown in Fig. 102.45 (open squares) for the cases where data are available. This temperature shows better agreement with simulation results.

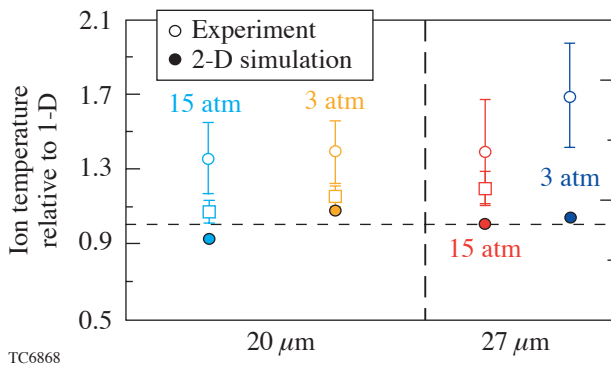


Figure 102.45
Neutron-averaged ion temperatures relative to 1-D for the four target configurations as in Fig. 102.43. Inferred ion temperatures from neutron time-of-flight (open circles) are systematically higher than simulated ion temperatures (solid circles). The ion temperatures inferred from the DD neutron to D³He proton yield ratios (open squares) are also shown.

The significant influence of low and intermediate wavelengths on thick shells is consistent with observations of neutron yields using the newer SG4 phase plates¹⁴ on the OMEGA laser beams. The improvement in the on-target laser nonuniformity between the SG3 and the SG4 phase plates has been modeled to be primarily in the low- and intermediate-mode ranges [Fig. 102.46(a)].¹⁴ The ratio of the calculated rms nonuniformity with the SG3 phase plates relative to the SG4 phase plates is shown in Fig. 102.46(a). In Fig. 102.46(b), the measured yield relative to 1-D is shown for both shell thicknesses. Significant improvement in the 27- μm -thick shell's performance is measured [Fig. 102.46(b)].

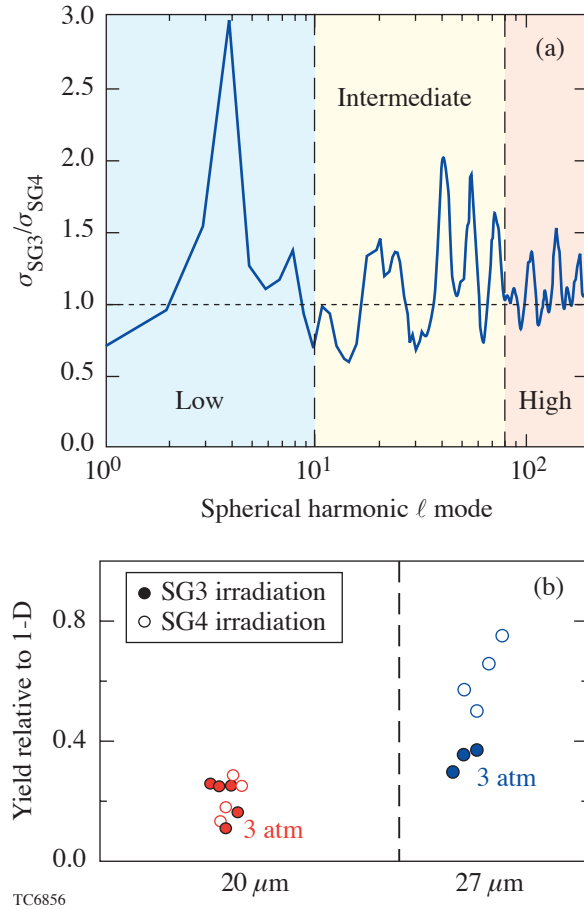


Figure 102.46
(a) Ratio of the modeled on-target laser nonuniformity due to the SG3 and SG4 phase plates (see text). Significant improvements in the uniformity of low and intermediate wavelengths have been modeled, whereas marginal improvements in the uniformity of short wavelengths are calculated. (b) Measured yields relative to 1-D for the SG3 phase plates (solid) and the SG4 phase plates (open) for 20- μm -thick and 27- μm -thick CH shells with 3-atm fills. Significant improvement is observed in target performance for the thicker shells unlike the thin shells. Thin-shell performance is dominated by the seeding of short-wavelength modes, which has marginally changed in the transition from SG3 to SG4 phase plates.

Lineouts from ~ 4.5 -keV gated x-ray pinhole camera images of the core self-emission for the 20- μm -thick CH shell are shown in Fig. 102.47. The results of Spect3D²⁹ post-processing of 2-D simulations (solid) with the 1-D results (dashed) are shown at peak neutron production [Fig. 102.47(a)] and at peak compression [Fig. 102.47(b)]. Each curve is normalized to the corresponding peak intensity. The postprocessed 1-D simulation shows a distinct limb corresponding to the fuel-shell interface position. The 2-D simulated emission in Figs. 102.47(a) and 102.47(b) is the polar angle average of the

emission from the target. The averaging process smears out the limb due to the nonuniformity of the fuel–shell interface. Further, peak simulated emission in 2-D occurs from the hot CH spikes, which are at a smaller radius than the 1-D fuel–shell interface (Fig. 102.39). As a result, the brightness profile in 2-D decreases rapidly at a smaller radius than in the 1-D emission profile. The more distorted shell also results in a more gradual decrease in the brightness compared to the 1-D profile. Comparisons of the measured azimuthally averaged curves¹⁸ normalized to peak intensity and the corresponding 1-D simulations are shown at peak neutron production [Fig. 102.47(c)] and at peak compression [Fig. 102.47(d)]. Similar trends are observed in experiments; the limb is no longer evident, the decrease in brightness occurs at a smaller radius than in 1-D, and this decrease is more gradual than in the 1-D profile.

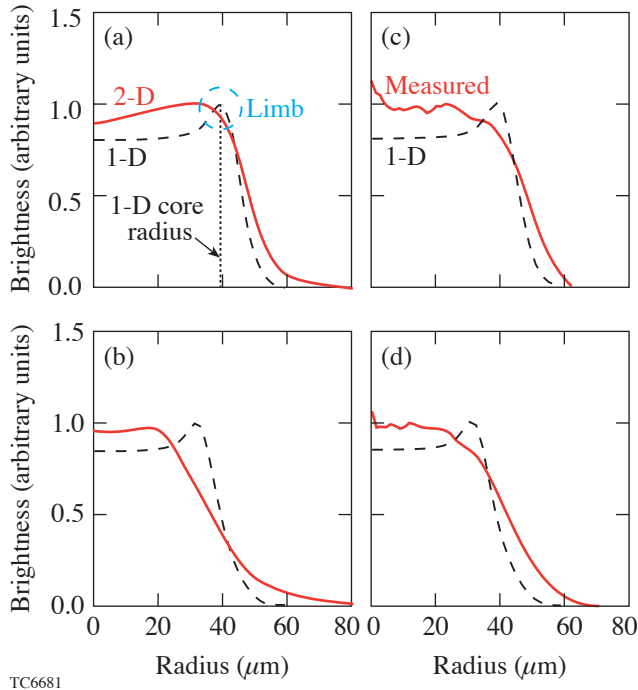


Figure 102.47

Brightness profile at ~ 4.5 keV of the core normalized to peak intensity for the 20- μm -thick CH shell. (a) Comparison of 1-D profiles (dashed) with the polar-averaged 2-D profile (solid) at peak neutron production. 1-D simulation indicates a prominent limb due to the fuel–shell interface. 2-D simulation indicates a smeared-out limb. (b) Same as (a) but at peak compression. (c) Azimuthally averaged brightness profile from measured pinhole camera images (shot 22546) at peak neutron production (solid line) compared to 1-D (dashed line). (d) Same as (c) but at peak compression. Good agreement is obtained between the 2-D profiles and the measured profiles including the absence of a significant limb and more gradual decrease in brightness relative to the 1-D profile.

In previous work, homogenous mixing of D_2 and CH^{30-33} has been inferred from experimental observables such as secondary neutron ratios,^{30,31} argon spectral lines,³² and D^3He yields in ^3He -filled CD shells.^{30,31} These observables preferentially sample the turbulently mixed region of the target and are sensitive to mix. The primary neutron yields were not directly used to determine the presence of turbulence. These neutrons are produced in the bulk of the fuel; the reduced values of the primary yields relative to 1-D are instead due to the effects discussed in **Effect of Shell Stability on Observables** (p. 95).

An order-of-magnitude estimate of the small-scale mixing length can be obtained as follows: The turbulent mixing layer grows self-similarly with a mixing thickness h , given by Ref. 34,

$$h = \alpha A_T g t^2, \quad (1)$$

where α is a dimensionless constant. Taking $A_T = 0.18$ for the D_2 –CH interface gives $\alpha = 0.05$ (Ref. 34). The expression in Ref. 34 is for planar turbulent growth due to the presence of many modes. In the cases considered in this article, convergence effects play an important role. In addition, the return shock recompresses the mixing layer. Subsequent reshocking of the mixing layer can occur in implosions; therefore, this estimate of mixing lengths should be considered as an order-of-magnitude estimate. A hydrodynamics code, such as *DRACO*, cannot follow materials into the turbulent regime. Using $\alpha = 0.05$ leads to $h = 0.9 \mu\text{m}$; therefore, if the simulated short-wavelength amplitude is considered to be a mix thickness, the value of $\sim 1 \mu\text{m}$ (Fig. 102.39) compares favorably with the estimated mix thickness. Larger mixing widths ($\sim 17 \mu\text{m}$) have been inferred based on spherically symmetric 1-D mix models.^{30,31} Since 1-D mix models do not account for the increased volume due to long-wavelength distortions, it is very likely that they overestimate the mixing length.

Conclusions

Two-dimensional simulations of imploding plastic shells are presented using the radiation hydrodynamic code *DRACO*. Shell instability through the growth of short-wavelength perturbations plays an important role in determining target performance for “thin” (≤ 20 - μm -thick) CH shells. Target performance is dominated by long and intermediate wavelengths for thicker shells. Observables such as primary neutron yields, areal densities, temporal histories of neutron production, and x-ray images of self-emission compare very well with experimental

measurements. Neutron-averaged ion temperatures inferred from neutron time of flight are significantly higher than the calculated values. The reasons for this systematic discrepancy are under investigation. Calculated ion temperatures, however, are more consistent with values inferred from the ratios of DD neutron to $D^3\text{He}$ proton yield. The good agreement with experiment for most observables indicates that the modeling of nonuniformity seeds for instability growth and multidimensional implosion dynamics due to realistic laser and target asymmetries describe realistic direct-drive inertial confinement fusion implosions reasonably well.

ACKNOWLEDGMENT

This work was supported by the U.S. Department of Energy Office of Inertial Confinement Fusion under Cooperative Agreement No. DE-FC52-92SF19460, the University of Rochester, and the New York State Energy Research and Development Authority. The support of DOE does not constitute an endorsement by DOE of the views expressed in this article.

REFERENCES

1. J. Nuckolls *et al.*, *Nature* **239**, 139 (1972).
2. Lord Rayleigh, *Proc. London Math Soc.* **XIV**, 170 (1883); G. Taylor, *Proc. R. Soc. London Ser. A* **201**, 192 (1950).
3. C. P. Verdon, *Bull. Am. Phys. Soc.* **38**, 2010 (1993); P. W. McKenty, V. N. Goncharov, R. P. J. Town, S. Skupsky, R. Betti, and R. L. McCrory, *Phys. Plasmas* **8**, 2315 (2001).
4. D. D. Meyerhofer, J. A. Delettrez, R. Epstein, V. Yu. Glebov, V. N. Goncharov, R. L. Keck, R. L. McCrory, P. W. McKenty, F. J. Marshall, P. B. Radha, S. P. Regan, S. Roberts, W. Seka, S. Skupsky, V. A. Smalyuk, C. Sorce, C. Stoeckl, J. M. Soures, R. P. J. Town, B. Yaakobi, J. D. Zuegel, J. Frenje, C. K. Li, R. D. Petrasso, D. G. Hicks, F. H. Séguin, K. Fletcher, S. Padelino, M. R. Freeman, N. Izumi, R. Lerche, T. W. Phillips, and T. C. Sangster, *Phys. Plasmas* **8**, 2251 (2001).
5. P. B. Radha, V. N. Goncharov, T. J. B. Collins, J. A. Delettrez, Y. Elbaz, V. Yu. Glebov, R. L. Keck, D. E. Keller, J. P. Knauer, J. A. Marozas, F. J. Marshall, P. W. McKenty, D. D. Meyerhofer, S. P. Regan, T. C. Sangster, D. Shvarts, S. Skupsky, Y. Srebro, R. P. J. Town, and C. Stoeckl, *Phys. Plasmas* **12**, 032702 (2005).
6. T. R. Boehly, D. L. Brown, R. S. Craxton, R. L. Keck, J. P. Knauer, J. H. Kelly, T. J. Kessler, S. A. Kumpan, S. J. Loucks, S. A. Letzring, F. J. Marshall, R. L. McCrory, S. F. B. Morse, W. Seka, J. M. Soures, and C. P. Verdon, *Opt. Commun.* **133**, 495 (1997).
7. J. D. Lindl, *Phys. Plasmas* **2**, 3933 (1995).
8. V. Lobatchev and R. Betti, *Phys. Rev. Lett.* **85**, 4522 (2000).
9. E. M. Campbell and W. J. Hogan, *Plasma Phys. Control. Fusion* **41**, B39 (1999).
10. W. R. Donaldson, R. Boni, R. L. Keck, and P. A. Jaanimagi, *Rev. Sci. Instrum.* **73**, 2606 (2002).
11. S. Skupsky, R. W. Short, T. Kessler, R. S. Craxton, S. Letzring, and J. M. Soures, *J. Appl. Phys.* **66**, 3456 (1989).
12. T. R. Boehly, V. A. Smalyuk, D. D. Meyerhofer, J. P. Knauer, D. K. Bradley, R. S. Craxton, M. J. Guardalben, S. Skupsky, and T. J. Kessler, *J. Appl. Phys.* **85**, 3444 (1999).
13. C. B. Burckhardt, *Appl. Opt.* **9**, 695 (1970); Y. Kato *et al.*, *Phys. Rev. Lett.* **53**, 1057 (1984); Laboratory for Laser Energetics LLE Review **65**, 1, NTIS document No. DOE/SF/19460-117 (1995). Copies may be obtained from the National Technical Information Service, Springfield, VA 22161.
14. S. P. Regan, J. A. Delettrez, V. Yu. Glebov, V. N. Goncharov, J. A. Marozas, F. J. Marshall, P. W. McKenty, D. D. Meyerhofer, P. B. Radha, T. C. Sangster, V. A. Smalyuk, C. Stoeckl, J. A. Frenje, C. K. Li, R. D. Petrasso, and F. H. Séguin, *Bull. Am. Phys. Soc.* **49**, 62 (2004).
15. C. K. Li, D. G. Hicks, F. H. Séguin, J. A. Frenje, R. D. Petrasso, J. M. Soures, P. B. Radha, V. Yu. Glebov, C. Stoeckl, D. R. Harding, J. P. Knauer, R. L. Kremens, F. J. Marshall, D. D. Meyerhofer, S. Skupsky, S. Roberts, C. Sorce, T. C. Sangster, T. W. Phillips, M. D. Cable, and R. J. Leeper, *Phys. Plasmas* **7**, 2578 (2000).
16. C. K. Li, F. H. Séguin, D. G. Hicks, J. A. Frenje, K. M. Green, S. Kurebayashi, R. D. Petrasso, D. D. Meyerhofer, J. M. Soures, V. Yu. Glebov, R. L. Keck, P. B. Radha, S. Roberts, W. Seka, S. Skupsky, C. Stoeckl, and T. C. Sangster, *Phys. Plasmas* **8**, 4902 (2001).
17. R. A. Lerche, D. W. Phillion, and G. L. Tietbohl, *Rev. Sci. Instrum.* **66**, 933 (1995).
18. S. P. Regan, J. A. Delettrez, R. Epstein, P. A. Jaanimagi, B. Yaakobi, V. A. Smalyuk, F. J. Marshall, D. D. Meyerhofer, W. Seka, D. A. Haynes, Jr., I. E. Golovkin, and C. F. Hooper, Jr., *Phys. Plasmas* **9**, 1357 (2002).
19. M. C. Richardson, G. G. Gregory, R. L. Keck, S. A. Letzring, R. S. Marjoribanks, F. J. Marshall, G. Pien, J. S. Wark, B. Yaakobi, P. D. Goldstone, A. Hauer, G. S. Stradling, F. Ameduri, B. L. Henke, and P. Jaanimagi, in *Laser Interaction and Related Plasma Phenomena*, edited by H. Hora and G. H. Miley (Plenum Press, New York, 1986), Vol. 7, pp. 179–211.
20. S. E. Bodner, *Phys. Rev. Lett.* **33**, 761 (1974); H. Takabe *et al.*, *Phys. Fluids* **28**, 3676 (1985); R. Betti, V. N. Goncharov, R. L. McCrory, P. Sorotokin, and C. P. Verdon, *Phys. Plasmas* **3**, 2122 (1996).
21. G. I. Bell, Los Alamos National Laboratory, Los Alamos, NM, Report LA-1321 (1951); M. S. Plesset, *J. Appl. Phys.* **25**, 96 (1954); D. L. Book and S. E. Bodner, *Phys. Fluids* **30**, 367 (1987); Laboratory for Laser Energetics LLE Review **94**, 81, NTIS document No. DOE/SF/19460-485 (2003). Copies of LLE Review **94** may be obtained from the National Technical Information Service, Springfield, VA 22161.
22. F. J. Marshall, J. A. Delettrez, R. Epstein, R. Forties, R. L. Keck, J. H. Kelly, P. W. McKenty, S. P. Regan, and L. J. Waxer, *Phys. Plasmas* **11**, 251 (2004).
23. K. A. Thorp, Laboratory for Laser Energetics, private communication (2004).

24. R. C. Cook, R. L. McEachern, and R. B. Stephens, *Fusion Technol.* **35**, 224 (1999).
25. V. N. Goncharov, S. Skupsky, T. R. Boehly, J. P. Knauer, P. McKenty, V. A. Smalyuk, R. P. J. Town, O. V. Gotchev, R. Betti, and D. D. Meyerhofer, *Phys. Plasmas* **7**, 2062 (2000).
26. R. Epstein, *J. Appl. Phys.* **82**, 2123 (1997).
27. V. N. Goncharov, P. McKenty, S. Skupsky, R. Betti, R. L. McCrory, and C. Cherfils-Clérouin, *Phys. Plasmas* **7**, 5118 (2000).
28. T. R. Boehly, V. N. Goncharov, O. Gotchev, J. P. Knauer, D. D. Meyerhofer, D. Oron, S. P. Regan, Y. Srebro, W. Seka, D. Shvarts, S. Skupsky, and V. A. Smalyuk, *Phys. Plasmas* **8**, 2331 (2001).
29. J. J. MacFarlane *et al.*, in *Inertial Fusion Sciences and Applications 2003*, edited by B. A. Hammel *et al.* (American Nuclear Society, La Grange Park, IL, 2004), pp. 457–460; Prism Computational Sciences, Inc., Madison, WI, 53711.
30. C. K. Li, F. H. Séguin, J. A. Frenje, S. Kurebayashi, R. D. Petrasso, D. D. Meyerhofer, J. M. Soures, J. A. Delettrez, V. Yu. Glebov, P. B. Radha, F. J. Marshall, S. P. Regan, S. Roberts, T. C. Sangster, and C. Stoeckl, *Phys. Rev. Lett.* **89**, 165002 (2002).
31. P. B. Radha, J. Delettrez, R. Epstein, V. Yu. Glebov, R. Keck, R. L. McCrory, P. McKenty, D. D. Meyerhofer, F. Marshall, S. P. Regan, S. Roberts, T. C. Sangster, W. Seka, S. Skupsky, V. Smalyuk, C. Sorce, C. Stoeckl, J. Soures, R. P. J. Town, B. Yaakobi, J. Frenje, C. K. Li, R. Petrasso, F. Séguin, K. Fletcher, S. Padalino, C. Freeman, N. Izumi, R. Lerche, and T. W. Phillips, *Phys. Plasmas* **9**, 2208 (2002).
32. S. P. Regan, J. A. Delettrez, V. N. Goncharov, F. J. Marshall, J. M. Soures, V. A. Smalyuk, P. B. Radha, B. Yaakobi, R. Epstein, V. Yu. Glebov, P. A. Jaanimagi, D. D. Meyerhofer, T. C. Sangster, W. Seka, S. Skupsky, C. Stoeckl, D. A. Haynes, Jr., J. A. Frenje, C. K. Li, R. D. Petrasso, and F. H. Séguin, *Phys. Rev. Lett.* **92**, 185002 (2004).
33. D. C. Wilson, C. W. Cranfill, C. Christensen, R. A. Forster, R. R. Peterson, H. M. Hoffman, G. D. Pollak, C. K. Li, F. H. Séguin, J. A. Frenje, R. D. Petrasso, P. W. McKenty, F. J. Marshall, V. Yu. Glebov, C. Stoeckl, G. J. Schmid, N. Izumi, and P. Amendt, *Phys. Plasmas* **11**, 2723 (2004).
34. G. Dimonte, *Phys. Plasmas* **6**, 2009 (1999).